



# Multiscale formulation of pore-scale compressible Darcy-Stokes flow



Bo Guo\*, Yashar Mehmani, Hamdi A. Tchelepi

Department of Energy Resources Engineering, Stanford University, 367 Panama St., Stanford, CA 94305-2220, USA

## ARTICLE INFO

### Article history:

Received 14 October 2018

Received in revised form 5 July 2019

Accepted 21 July 2019

Available online 25 July 2019

### Keywords:

Porous media

Multiscale method

Pore-scale modeling

Darcy-Stokes flow

Compressible flow

Microporosity

## ABSTRACT

Direct numerical simulation (DNS) of fluid dynamics in digital images of porous materials is challenging due to the cut-off length issue where interstitial voids below the resolution of the imaging instrument cannot be resolved. Such subresolution microporosity can be critical for flow and transport because they could provide important flow pathways. A micro-continuum framework can be used to address this problem, which applies to the entire domain a single momentum equation, i.e., Darcy-Brinkman-Stokes (DBS) equation, that recovers Stokes equation in the resolved void space (i.e., macropores) and Darcy equation in the microporous regions. However, the DBS-based micro-continuum framework is computationally demanding. Here, we develop an efficient multiscale method for the compressible Darcy-Stokes flow arising from the micro-continuum approach. The method decomposes the domain into subdomains that either belong to the macropores or the microporous regions, on which Stokes or Darcy problems are solved locally, only once, to build basis functions. The nonlinearity from compressible flow is accounted for in a local correction problem on each subdomain. A global interface problem is solved to couple the local bases and correction functions to obtain an approximate global multiscale solution, which is in excellent agreement with the reference single-scale solution. The multiscale solution can be improved through an iterative strategy that guarantees convergence to the single-scale solution. The method is computationally efficient and well-suited for parallelization to simulate fluid dynamics in large high-resolution digital images of porous materials.

© 2019 Elsevier Inc. All rights reserved.

## 1. Introduction

Fluid flow and transport in porous media play a fundamental role in a broad range of geoscience and industrial applications, such as contaminant transport in groundwater, hydrocarbon production, geological carbon sequestration, fuel cells, and inkjet paper printing. It is critical to understand flow and transport processes at the pore scale (i.e., the scale of the interstices between the solid grains) because they govern the overall macroscopic behavior of fluids in the porous material. In geoscience applications, the so-called Digital Rock Physics (DRP) has emerged as a routinely used technology to study fluid dynamics in rocks at the pore scale [1–3]. DRP involves using imaging instruments (e.g., X-ray micro-CT, Scanning Electron Microscopy (SEM)) to acquire digital images of rock samples and performing simulations of fluid flow through the digitized pore structures to compute macroscopic properties (e.g., permeability). Largely, two classes of methods are used

\* Corresponding author. Now at the Department of Hydrology and Atmospheric Sciences, University of Arizona, USA.

E-mail addresses: boguo@email.arizona.edu (B. Guo), ymehmani@stanford.edu (Y. Mehmani), tchelepi@stanford.edu (H.A. Tchelepi).

for flow simulations: Pore Network Modeling (PNM) and Direct Numerical Simulation (DNS). PNM is a simplified approach that approximates the rock pore structures with interconnected pore throats and pore bodies, in which flow and transport equations are solved. PNM is very computationally efficient, but it yields an approximate solution with errors that are difficult to estimate *a priori*. DNS, such as, finite volume or element methods, directly discretizes the pore geometry and solves the equations for flow and transport. DNS is accurate given enough spatial and temporal resolution, but it is very computationally demanding, especially for large high-resolution images. In this work, we focus on the DNS solution of the Navier-Stokes equations.

A challenge for simulating flow on digital images of geological porous materials is the issue of cut-off length, i.e., interstitial voids below the resolution of the imaging instruments cannot be resolved. For reservoir rocks, e.g., carbonate, subresolution microporosity has been shown to be critical for flow and transport by both PNM [4,5] and DNS studies [6,7]. Microporosity can also be quantified experimentally using differential imaging with high-salinity contrast brine [8]. To address the cut-off length issue for reservoir rocks, Soulaire and Tchelepi [9] developed a micro-continuum DNS modeling framework based on the Darcy-Brinkman-Stokes (DBS) equation [10] where the Stokes flow is solved in the resolved macropores while Darcy flow is solved in the regions with microporosity. The cut-off length problem becomes even more challenging for unconventional organic-rich shale rocks, because the majority of the pores are in the range of a few to tens of nanometers that may be below the resolution of micro-CT or SEM images (e.g., [11–13]). These nanometer-scale pores are critical for flow and transport because inside them many physical processes take place (e.g., Knudsen diffusion, slip flow, adsorption/desorption, and surface diffusion). Guo et al. [14] developed a micro-continuum model for gas transport in organic-rich shales accounting for the various physical processes in the subresolution nanoporous regions. The DBS-based micro-continuum modeling framework is a useful DNS method, but it is computationally demanding for simulations on high-resolution images of statistically representative large rock samples. Accelerating computation of the micro-continuum framework is therefore critical.

There are relatively few reports on accelerating DNS by means of a multiscale formulation. One class of methods builds upon the multiscale finite volume (MsFV) method developed at the Darcy scale for reservoir simulation (e.g., [15,16]). Tomin and Lunati [17] developed a hybrid method for two-phase flow where a coarse-scale problem is formulated using the MsFV at the Darcy scale and the Navier-Stokes equation is solved in subdomains that contain many pores. Multiscale formulations have also been developed for PNM. Khayrat and Jenny [18] developed a multiscale method using the MsFV framework, similar to Tomin and Lunati [17], while the subdomain problems are solved using PNM. In the framework of mortar domain decomposition [19–21], multiscale methods that couple PNM to Darcy-scale models for single-phase flow and transport have been developed [22–24]. Recently, Mehmani and Tchelepi [25] developed a new pore-level multiscale method (PLMM) for single-phase incompressible Navier-Stokes flow. It decomposes the pore space into subdomains that coincide with physical pores in the void space and builds local basis functions on them. These local bases are coupled through a global interface problem to obtain an approximate solution, which can then be improved with an iterative strategy that guarantees convergence to the DNS solution. PLMM has recently been extended to two-phase incompressible Navier-Stokes flow at the pore scale [26]. A discussion of the differences and links of the different pore-scale multiscale methods and PNM can be found in [25].

Here, we extend the PLMM of [25] and develop a multiscale formulation for compressible Darcy-Stokes flow in porous materials with microporosity. We aim to develop an algorithm that can efficiently compute compressible Darcy-Stokes flow at the pore scale with controllable accuracy. We consider a segmented ternary digital rock image that consists of macropores, subresolution microporous regions, and non-porous solids (see Fig. 1a). The flow in the macropores is modeled as Stokes flow, while the subresolution microporous region is modeled as Darcy flow. The decomposition generalizes that in [25] and partitions the macropores and the microporous regions into subdomains, which either belong to the macropores or the microporous region (see Fig. 1b).

We consider compressible flow with pressure-dependent density. This leads to a nonlinear continuity equation, which we linearize using the iteration scheme reported in [27] in the context of compressible MsFV. We build local bases, only once, for velocity and pressure in each subdomain by solving the Stokes or Darcy equations. The inhomogeneous terms of the continuity equation are accounted for in a correction problem with homogeneous boundary conditions (BC) in each of the subdomains. We solve a global problem by imposing continuity of mass flowrate at the interfaces between the subdomains to obtain the multipliers for the local bases. Superimposing the local bases and the correction functions leads to a global fine-scale solution, which is an approximate solution because the local BCs used to build the bases are not exact. The error can be eliminated through an iterative correction scheme similar to [25]. We do so by solving local problems in the neighborhood of the subdomain interfaces to correct the local BCs. The updated local BCs are then used in the correction problems. With such corrective iterations, the multiscale solution converges to the DNS solution. The iterative correction is very efficient, and we show that one iteration reduces the error by roughly an order of magnitude.

We structure the paper as follows. In section 2, we describe the problem for compressible flow in a ternary image with microporosity and introduce the governing equations. In section 3, we present the multiscale formulation and algorithm for compressible Darcy-Stokes flow. The formulation and algorithm for incompressible flow is presented as a special case. Following that, in section 4, we show results from three test cases and compare the multiscale solution with the reference single-scale solution. In section 5, we discuss the computational cost and accuracy of the multiscale method, the coupling conditions at the interface between Darcy and Stokes flow, and future directions. We close in section 6 with concluding remarks.

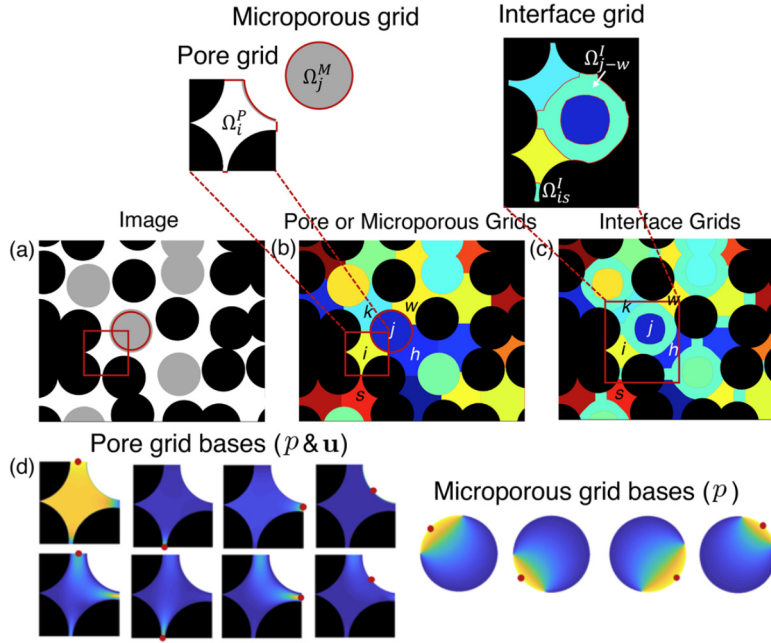


**Fig. 1.** Schematic of the multiscale method for compressible Darcy-Stokes flow. (a) A ternary image in which white, gray, and black colors denote macropores, microporous regions, and non-porous solids, respectively; an example of a pore grid and a microporous grid after the image is decomposed is marked by a red rectangle and a red circle, respectively. (b) The decomposed coarse pore and microporous grids. The pore and microporous grids marked in (a) are shown as an example of the individual coarse grids in the inset. (c) The interface grids shown on top of the decomposed pore and microporous grids with examples of the interface grids shown in the inset.  $\Omega_{j-w}^I$  denotes  $\Omega_{j,h,i,k,w}^I$  representing a merged interface grid. (d) Schematic of the basis functions for a pore grid and a microporous grid. (For interpretation of the colors in the figure(s), the reader is referred to the web version of this article.)

## 2. Problem description and single-scale modeling

We consider a ternary segmented image ( $\Omega$ ) of a rock sample that consists of macropores ( $\Omega^P$ ), microporous regions ( $\Omega^M$ ) where each voxel is an aggregation of void and solid, and non-porous solids ( $\Omega^S$ ). Fig. 1(a) shows an example of a 2D ternary image. We consider compressible single-phase flow in the rock sample through the macropores ( $\Omega^P$ ) and the microporous regions ( $\Omega^M$ ). The flow in the macropores can be described by the Stokes equation, while the microporous regions can be considered as a continuum, in which the fluid flow can be described by the Darcy equation. A micro-continuum framework based on the DBS equations can be used to model fluid flow [10,28,29,9,14]. Further discussions on the coupling condition between free flow-porous media interfaces are provided in section 5. The continuity and momentum equations for single-phase compressible flow have the following forms

$$\phi \frac{\partial \rho}{\partial t} + \nabla \cdot (\rho \mathbf{u}) = 0, \quad (1)$$

$$0 = -\nabla p + \frac{\mu}{\phi} \nabla \cdot (\nabla \mathbf{u}) + \frac{\mu}{3\phi} \nabla (\nabla \cdot \mathbf{u}) - \mathbf{k}^{-1} \mu \mathbf{u}, \quad (2)$$

where  $\rho$  is density,  $\mu$  is dynamic viscosity which is assumed to be constant,  $\mathbf{u}$  is velocity, and  $p$  is pressure.  $t$  is time.  $\phi$  is porosity and  $\mathbf{k}$  is the permeability tensor of the microporous regions of the rock. The momentum Eq. (2) recovers the Stokes equation in the macropores when  $\phi = 1$  and  $\mathbf{k}^{-1} = 0$ , and it recovers the Darcy equation in the microporous regions when  $0 < \phi < 1$ . Note that all terms in Eq. (2) are retained when  $0 < \phi < 1$ , but the Darcy term is predominant. Similarly, the continuity equation recovers the continuity equations for free flow in the macropores when  $\phi = 1$  and for Darcy flow in the microporous regions when  $0 < \phi < 1$ .

We discretize and solve Eqs. (1) and (2) in the macropores and the microporous regions ( $\Omega^P \cup \Omega^M$ ) of the rock subject to a no-slip condition at non-porous solid walls  $\Gamma_w = (\partial \Omega^P \cap \partial \Omega^S) \cup (\partial \Omega^M \cap \partial \Omega^S)$ , and BCs at the external boundaries of the image. Unless stated otherwise, the numerical grid cells have a one-to-one correspondence to the voxels in the image. We refer to these grid cells as *fine-scale* grids.  $\phi$  is used as an indicator where the image voxels in the macropores have  $\phi = 1$  and the ones in the microporous regions have  $\phi$  as the average porosity for subresolution pores in a pixel. Eqs. (1) and (2) are solved using the extended SIMPLEC (Semi-Implicit Method for Pressure Linked Equations-Consistent) algorithm for compressible flow [30,31]. We refer to the fine-scale solution with no domain decomposition as the single-scale solution, which we use as a reference to compare with the multiscale solution in section 3.

### 3. Multiscale modeling

We develop a multiscale method to solve compressible single-phase flow in a ternary digital rock image. The multiscale method is designed to approximate the single-scale DNS solution efficiently with controllable accuracy. We first present a general multiscale formulation for compressible flow, and then discuss incompressible flow as a special case.

#### 3.1. Linearization of the continuity equation

To solve the nonlinear equations for compressible flow in a multiscale framework, we linearize the continuity equation. The linearization is done in a semi-discrete form following [27], which was introduced in the context of the MsFV method.

Discretizing Eq. (1) in time and dividing both sides by  $\rho^{n+1}$ , we obtain the semi-discrete equation

$$\frac{\phi}{\Delta t} - \frac{\phi \rho^n}{\Delta t} \frac{1}{\rho^{n+1}} + \frac{1}{\rho^{n+1}} \nabla \cdot (\rho^{n+1} \mathbf{u}^{n+1}) = 0, \quad (3)$$

where  $\Delta t$  is the time step size, and  $n$  denotes the time step.

Eq. (3) is nonlinear and can be solved iteratively by introducing the following iteration scheme

$$\frac{\phi}{\Delta t} - \frac{\phi \rho^n}{\Delta t} \frac{1}{\rho^{m+1}} + \frac{1}{\rho^{m+1}} \nabla \cdot (\rho^{m+1} \mathbf{u}^{m+1}) = 0. \quad (4)$$

Approximating  $1/\rho^{m+1}$  using the first-order Taylor expansion yields

$$\frac{\phi}{\Delta t} - \frac{\phi \rho^n}{\Delta t} \left[ \frac{1}{\rho^m} + \left( \frac{\partial (1/\rho)}{\partial p} \right)^m (p^{m+1} - p^m) \right] + \frac{1}{\rho^{m+1}} \nabla \cdot (\rho^{m+1} \mathbf{u}^{m+1}) = 0. \quad (5)$$

Using the discretization  $1/\rho^{m+1} \nabla \cdot (\rho^{m+1} \mathbf{u}^{m+1}) \approx \nabla \cdot \mathbf{u}^{m+1} - \nabla \cdot \mathbf{u}^m + 1/\rho^m \nabla \cdot (\rho^m \mathbf{u}^m)$ , we obtain

$$\frac{C}{\Delta t} p^{m+1} + \nabla \cdot \mathbf{u}^{m+1} = RHS^m + \frac{C}{\Delta t} p^m, \quad (6)$$

where  $C = -\phi \rho^n \left( \frac{\partial (1/\rho)}{\partial p} \right)^m$ ,  $RHS^m = -\frac{\phi}{\Delta t} + \frac{\phi \rho^n}{\Delta t} \frac{1}{\rho^m} + \nabla \cdot \mathbf{u}^m - \frac{1}{\rho^m} \nabla \cdot (\rho^m \mathbf{u}^m)$ . We note that  $C$  only influences the rate of convergence, and does not affect the final converged solution. Thus, there is some flexibility to choose  $C$  as long as it maintains fast convergence. In the results presented in this paper, we choose  $C = -\phi \rho^0 \left( \frac{\partial (1/\rho)}{\partial p} \right)^0$  where  $\rho^0$  and  $\left( \frac{\partial (1/\rho)}{\partial p} \right)^0$  are computed with the density and pressure at the initial condition. Eq. (6) is the linearized continuity equation that we will use in the multiscale formulation.

#### 3.2. Domain decomposition

We decompose a ternary image (see a 2D example in Fig. 1(a)) into non-overlapping subdomains (Fig. 1(b)). The domain decomposition generalizes [25] and applies watershed transform [32] separately to  $\Omega^P$  and  $\Omega^M$ , leading to decomposed macropores and microporous subdomains. The decomposed macropores are referred to as pore grids ( $\Omega_i^P$ ), and the decomposed microporous subdomains are referred to as microporous grids ( $\Omega_i^M$ ).  $\Omega_i^P$  and  $\Omega_i^M$  are the *coarse-scale* subdomains that are comprised of several *fine-scale* grids defined in section 2. We use the term “coarse grid” and “subdomain” interchangeably in the rest of the paper. Note that when we decompose the images, we include a thin layer from the microporous regions ( $\Omega^M$ ) into the macropore regions ( $\Omega^P$ ) so that the interface between  $\Omega^P$  and  $\Omega^M$  always resides in  $\Omega_i^P$ . This is done by performing successive morphological dilations of  $\Omega^P$  using a structuring element that is either a disk (2D) or a sphere (3D) of one-pixel radius [33]. We perform three dilations here. As a result, the interfaces between free flow and porous medium are always inside pore grids  $\Omega_i^P$  (see the inset of Fig. 1(b)). This allows better initial approximations of the local boundary conditions for the interfaces between  $\Omega_i^P$  and  $\Omega_i^M$  subdomains (sections 3.3.1 and 3.3.2).

In addition to pore and microporous grids, we define another set of coarse grids, referred to as interface grids (similar to “throat grids” in [25]). Each interface grid ( $\Omega_{ij}^I$ ) is created to cover a neighborhood around the interface between two subdomains  $\Omega_i^X$  and  $\Omega_j^X$ . The superscript  $X$  denotes  $P$  or  $M$  representing a pore grid or a microporous grid, respectively. We use this convention in the rest of the paper.  $N_X$  is used to denote the total number of subdomains. We create interface grids by performing successive morphological dilations of the voxels constituting the subdomain interfaces. The number of dilations,  $N_D$ , determines the width of interface grids and is a user-defined parameter.  $N_D$  is chosen as 8 or 16 in this paper. Note that interface grids do not fully cover  $\Omega^P \cup \Omega^M$ . The total number of interface grids is  $N_I$ . Note that interface grids can overlap with adjacent interface grids, in which case they are merged (e.g.,  $\Omega_{j-w}^I$  in the inset of Fig. 1(c); see [25] for details). Thus, the total number of interface grids may be less than  $N_I$  due to merger.

We define the neighboring subdomains of  $\Omega_i^X$  as those  $\Omega_j^X$  with which it shares a common interface  $\Gamma_{ij}^{XX}$ . We use  $I_i$  and  $N_i$  to denote the index set and the number of the neighbor subdomains of  $\Omega_i^X$ .  $\partial \Omega_i^X$ , the external boundary of  $\Omega_i^X$ , includes

a fluid-solid interface ( $X = P$ ) or a porous medium-solid interface ( $X = M$ ),  $\Gamma_{i,w}^X = \partial\Omega_i^X \cap \Gamma_w$ , and interfaces between  $\Omega_i^X$  and its neighbors  $\Omega_j^X$ ,  $\Gamma_{ij}^{XX} = \partial\Omega_i^X \cap \partial\Omega_j^X \forall j \in I_i$  (see Fig. 1(b)). We define a constant normal vector  $\mathbf{n}$  for each  $\Gamma_{ij}^{XX}$  which is the average of the normal vectors along  $\Gamma_{ij}^{XX}$ . Similarly, the interface grids also have  $\Gamma_{i,w}^I$  and  $\Gamma_{ij}^I$ . Note that  $\Gamma_{ij}^I$  may consist of disconnected segments (see the inset of Fig. 1(c)). A constant normal vector is defined on each segment of  $\Gamma_{ij}^I$ . Note that the decomposed subdomains  $\Omega_i^X$  are directly used for the multiscale computations (sections 3.3–3.6)—no assumptions about the geometry of  $\Omega_i^X$  and the interfaces  $\Gamma_{ij}^{XX}$  are imposed.

### 3.3. Local basis problems

We use the term *local* to refer to problems on a single coarse grid and *global* for problems defined on the entire permeable domain ( $\Omega^P \cup \Omega^M$ ). Superscripts  $f$  and  $c$  are used to denote fine- and coarse-scale variables, respectively. In this section, our goal is to solve local problems on each coarse grid. Since the BCs are not known *a priori*, we make the following approximation by assuming, along an interface ( $\Gamma_{ij}^{XX}$ ) between two subdomains, the normal stress is zero (for pore grids) and the pressure is constant

$$\partial_{\mathbf{n}} \mathbf{u}^f|_{\Gamma_{ij}^{XX}} = 0, \quad (7)$$

$$p^f|_{\Gamma_{ij}^{XX}} = p_{ij}^c, \quad (8)$$

where  $p_{ij}^c$  is a pressure value over the interface  $\Gamma_{ij}^{XX}$ . By definition,  $p_{ij}^c = p_{ji}^c$ . The fluid-solid interface (for pore grids)  $\Gamma_{i,w}^P$  or the porous medium-solid interface (for microporous grids)  $\Gamma_{i,w}^M$  is considered as wall. We can solve the local problems and superimpose the local solutions to construct an approximate global fine-scale solution, if  $[p_{ij}^c]_{N_I \times 1}$  is known. In the following, we introduce the local basis problems for both the pore grid ( $\Omega_i^P$ ) and the microporous grid ( $\Omega_i^M$ ) that give the local solutions. In section 3.4, we introduce a global interface problem to obtain  $[p_{ij}^c]_{N_I \times 1}$ .

#### 3.3.1. Pore grid

Note that pore grids that share interfaces with microporous grids contain a thin layer of  $\Omega_m$  after the decomposition (see the inset of Fig. 1(b)). Thus, we use Eqs. (1) and (2) to describe fluid flow in a pore grid ( $\Omega_i^P$ ), which accounts for the microporous layer with a porosity indicator. We define the following local basis problem

$$\frac{C}{\Delta t} \varphi_{ik}^{f,P} + \nabla \cdot \boldsymbol{\psi}_{ik}^{f,P} = 0, \quad (9)$$

$$0 = -\nabla \varphi_{ik}^{f,P} + \frac{\mu}{\phi} \nabla \cdot (\nabla \boldsymbol{\psi}_{ik}^{f,P}) + \frac{\mu}{3\phi} \nabla (\nabla \cdot \boldsymbol{\psi}_{ik}^{f,P}) - \mathbf{k}^{-1} \mu \boldsymbol{\psi}_{ik}^{f,P}, \quad (10)$$

subject to the BCs

$$\partial_{\mathbf{n}} \boldsymbol{\psi}_{ik}^{f,P}|_{\Gamma_{ij}^{PX}} = 0, \quad (11)$$

$$\varphi_{ik}^{f,P}|_{\Gamma_{ij}^{PX}} = \delta_{kj}, \quad (12)$$

where  $\boldsymbol{\psi}_{ik}^{f,P}$  and  $\varphi_{ik}^{f,P}$  are the basis functions for velocity and pressure, respectively. The subscript  $k$  denotes the index of the neighboring grids  $\Omega_j^X$  of  $\Omega_i^P$ , which is either a pore grid  $\Omega_j^P$  or a microporous grid  $\Omega_j^M$ .  $\delta_{kj}$  is the Kronecker delta.  $\Gamma_{ij}^{PX}$  is the boundary of the pore grid ( $\Omega_i^P$ ) adjacent to  $\Omega_j^X$ .

In addition to the basis problem, we need a correction problem to account for the inhomogeneous terms in the continuity Eq. (6). Eqs. (13)–(14) and the BCs Eqs. (15)–(16) define the correction problem.

$$\frac{C}{\Delta t} \tilde{\varphi}_i^{f,P,m+1} + \nabla \cdot \tilde{\boldsymbol{\psi}}_i^{f,P,m+1} = RHS^{f,m} + \frac{C}{\Delta t} p^{f,m}, \quad (13)$$

$$0 = -\nabla \tilde{\varphi}_i^{f,P,m+1} + \frac{\mu}{\phi} \nabla \cdot (\nabla \tilde{\boldsymbol{\psi}}_i^{f,P,m+1}) + \frac{\mu}{3\phi} \nabla (\nabla \cdot \tilde{\boldsymbol{\psi}}_i^{f,P,m+1}) - \mathbf{k}^{-1} \mu \tilde{\boldsymbol{\psi}}_i^{f,P,m+1}, \quad (14)$$

subject to the homogeneous BCs

$$\partial_{\mathbf{n}} \tilde{\boldsymbol{\psi}}_i^{f,P,m+1}|_{\Gamma_{ij}^{PX}} = 0, \quad (15)$$

$$\tilde{\varphi}_i^{f,P,m+1}|_{\Gamma_{ij}^{PX}} = 0, \quad (16)$$

where  $\tilde{\boldsymbol{\psi}}_i^{f,P,m+1}$  and  $\tilde{\varphi}_i^{f,P,m+1}$  denote the correction solutions for velocity and pressure at iteration  $m+1$ , respectively.  $RHS^{f,m}$  and  $p^{f,m}$  are from the fine-scale solutions at iteration  $m$ , as defined in Eq. (6).

### 3.3.2. Microporous grid

For microporous grids, the continuity equation is the same as Eq. (1). The momentum balance is modeled using the Darcy equation

$$\mathbf{u} = -\frac{\mathbf{k}}{\mu} \nabla p. \quad (17)$$

Eqs. (18)–(19) and the BCs Eq. (20) define the local basis problem for the microporous grid  $\Omega_i^M$ .

$$\frac{C}{\Delta t} \varphi_{ik}^{f,M} + \nabla \cdot \boldsymbol{\psi}_{ik}^{f,M} = 0, \quad (18)$$

$$\boldsymbol{\psi}_{ik}^{f,M} = -\frac{\mathbf{k}}{\mu} \nabla \varphi_{ik}^{f,M}, \quad (19)$$

subject to the BCs

$$\varphi_{ik}^{f,M} |_{\Gamma_{ij}^{MX}} = \delta_{kj}, \quad (20)$$

$\boldsymbol{\psi}_{ik}^{f,M}$  and  $\varphi_{ik}^{f,M}$  denote the basis functions for velocity and pressure, respectively. The subscript  $k$  denotes the index of the neighboring grid  $\Omega_j^X$  of the microporous grid  $\Omega_i^M$ ;  $\Gamma_{ij}^{MX}$  is the boundary of the microporous grid ( $\Omega_i^M$ ) adjacent to  $\Omega_j^X$ .

Similar to pore grids, we need a correction problem to account for the inhomogeneous terms in the continuity Eq. (6). Eqs. (21)–(22) and the BCs Eq. (23) define the correction problem.

$$\frac{C}{\Delta t} \tilde{\varphi}_i^{f,M,m+1} + \nabla \cdot \tilde{\boldsymbol{\psi}}_i^{f,M,m+1} = RHS^{f,m} + \frac{C}{\Delta t} p^{f,m}, \quad (21)$$

$$\tilde{\boldsymbol{\psi}}_i^{f,M,m+1} = -\frac{\mathbf{k}}{\mu} \nabla \tilde{\varphi}_i^{f,M,m+1}, \quad (22)$$

subject to the homogeneous BCs

$$\tilde{\varphi}_i^{f,M,m+1} |_{\Gamma_{ij}^{MX}} = 0, \quad (23)$$

where  $\tilde{\boldsymbol{\psi}}_i^{f,M,m+1}$  and  $\tilde{\varphi}_i^{f,M,m+1}$  denote the correction solutions for velocity and pressure for iteration  $m+1$ , respectively.

### 3.4. Global problem

We formulate a global interface problem to couple the local basis and correction problems to obtain the multipliers  $[p_{ij}^c]_{N_i \times 1}$ . This is almost identical to the global interface problem formulated in [25] for single-phase incompressible flow. Here, we impose continuity of mass flowrate at the interfaces between subdomains because flow is compressible.

Each coarse grid  $\Omega_i^X$  has  $N_i$  basis functions  $\Psi_{ik}^{f,X} \equiv \{\boldsymbol{\psi}_{ik}^{f,X}, \varphi_{ik}^{f,X}\}$ . We compute the mass flowrate across the boundary  $\Gamma_{ij}^{XX}$  of  $\Omega_i^X$  for each basis function  $\Psi_{ik}^{f,X}$  as

$$q_{ij}^{c,k} = \int_{\Gamma_{ij}^{XX}} \rho \boldsymbol{\psi}_{ik}^f \cdot \mathbf{n} \, ds \quad \forall k \in I_i. \quad (24)$$

With the  $N_i$  basis functions  $\Psi_{ik}^{f,X}$  for  $\Omega_i^X \, \forall k \in I_i$ , the mass flowrates form a matrix

$$G_i^c = \begin{bmatrix} q_{ij_1}^{c,k_1} & q_{ij_1}^{c,k_2} & \cdots \\ q_{ij_2}^{c,k_1} & q_{ij_2}^{c,k_2} & \cdots \\ \vdots & \vdots & \cdots \end{bmatrix}_{N_i \times N_i}. \quad (25)$$

$G_i^c$  can be viewed as a flow response operator for  $\Omega_i^X$ . The  $l^{th}$  column of  $G_i^c$ ,  $[q_{ij_1}^{c,k_l}, q_{ij_2}^{c,k_l}, \dots]_{N_i \times 1}^T$ , corresponds to the basis solution  $\Psi_{ik_l}^{f,X}$  with  $k_l \in I_i$ . Given arbitrary  $[p_{ij}^c]_{N_i \times 1}$ , we define the mass flowrates entering or exiting  $\Omega_i^X$  through  $\Gamma_{ij_l}^{XX}$ , with  $l \in [1, N_i]$ , as

$$Q_i^c = [q_{ij_1}^c, q_{ij_2}^c, \dots]_{N_i \times 1}^T \quad (26)$$



The mass flowrates across the interfaces at iteration level  $m + 1$  are then obtained from

$$Q_i^{c,m+1} = G_i^c P_i^c + \tilde{Q}_i^{c,m+1}, \quad (27)$$

where

$$P_i^c = [p_{ij_1}^c, p_{ij_2}^c, \dots]^T_{N_l \times 1}, \quad (28)$$

$$\tilde{Q}_i^{c,m+1} = [\tilde{q}_{ij_1}^{c,m+1}, \tilde{q}_{ij_2}^{c,m+1}, \dots]^T_{N_l \times 1}. \quad (29)$$

$P_i^c$  is the vector of the pressures  $p_{ij_l}^c$  at  $\Gamma_{ij_l}^{XX}$  ( $l \in [1, N_l]$  and  $j_l \in J_i$ ). Note that  $P_i^c$  is a subset of  $[p_{ij}^c]_{N_l \times 1}$ .  $\tilde{q}_{ij_l}^{c,m+1}$  is the mass flowrate entering or exiting  $\Omega_i^X$  through  $\Gamma_{ij_l}^{XX}$  for  $l \in [1, N_l]$  corresponding to the correction solutions of Eqs. (13)–(14) and (21)–(22) at iteration  $m + 1$ .

Continuity of mass flowrate at subdomain interfaces gives

$$q_{ij}^{c,m+1} = q_{ji}^{c,m+1} \quad \forall ij. \quad (30)$$

Note that  $q_{ij}^{c,m+1} \neq q_{ji}^{c,m+1}$  for arbitrary  $p_{ij}^c$ . Continuity of mass flowrates at all the interfaces leads to a global linear system

$$G^c [p_{ij}^c]_{N_l \times 1} = F^{c,b} + \tilde{F}^{c,m+1} \quad \forall ij, \quad (31)$$

where  $G^c$  is a  $N_l \times N_l$  matrix that consists of the elements of  $G_i^c$  for each  $\Omega_i^X$ ,  $[p_{ij}^c]_{N_l \times 1}$  corresponds to the pressure values at the  $N_l$  interfaces,  $F^{c,b}$  and  $\tilde{F}^{c,m+1}$  are the  $N_l \times 1$  right-hand side (RHS) vectors due to the BCs and the correction solutions, respectively. Solving the linear system Eq. (31) yields  $[p_{ij}^c]_{N_l \times 1}$ , with which we construct the global fine-scale solution at iteration  $m + 1$

$$\mathbf{u}^{f,m+1} = \sum_{\forall i} \left( \sum_{k \in I_i} p_{ik}^c \psi_{ik}^{f,X} + \tilde{\psi}_i^{f,X,m+1} \right), \quad (32)$$

$$p^{f,m+1} = \sum_{\forall i} \left( \sum_{k \in I_i} p_{ik}^c \phi_{ik}^{f,X} + \tilde{\phi}_i^{f,X,m+1} \right), \quad (33)$$

Given  $\mathbf{u}^{f,m+1}$  and  $p^{f,m+1}$ , we repeat the above procedure to update solutions at the next iteration level. This involves solving the correction problems Eqs. (13)–(14) and (21)–(22) and the global interface problem. We iterate until a converged solution is obtained satisfying the criterion  $\|p^{f,m+1} - p^{f,m}\|_\infty < \epsilon$ , where  $\epsilon$  is the tolerance. A tolerance of  $\epsilon = 10^{-8}$  is used in our test cases in section 4. We have observed that less than 3 iterations are needed to achieve convergence. The global fine-scale solution Eq. (32)–(33) is an approximation to DNS because the local BCs used in the local problems are not exact. We refer to this approximate solution as the single-pass multiscale solution, denoted by  $M_0$ . In the next section, we introduce an iterative scheme to correct the local BCs so that the multiscale solution converges to the single-scale solution.

### 3.5. Iterative correction of local boundary conditions

The BCs used to solve the local basis problems in section 3.3 are not exact, which can lead to errors near the interfaces between coarse grids. Here, we solve local problems around subdomain interfaces to correct the local BCs in Eqs. (11)–(12) and Eq. (20). We use Eqs. (1) and (2) because the interface grids overlap with either pore grids or microporous grids. Using  $\hat{\mathbf{u}}_{ij}^f$  and  $\hat{p}_{ij}^f$  to denote the solutions on the interface grid  $\Omega_{ij}^l$ , and assuming the global fine-scale solutions  $\mathbf{u}^{f,m}$  and  $p^{f,m}$  are known at iteration  $m$ , we solve the following local problem on  $\Omega_{ij}^l$

$$\phi \frac{\partial \hat{\rho}_{ij}^{f,m}}{\partial t} + \nabla \cdot (\hat{\rho}_{ij}^{f,m} \hat{\mathbf{u}}_{ij}^{f,m}) = 0, \quad (34)$$

$$0 = -\nabla \hat{p}_{ij}^{f,m} + \frac{\mu}{\phi} \nabla \cdot (\nabla \hat{\mathbf{u}}_{ij}^{f,m}) + \frac{\mu}{3\phi} \nabla (\nabla \cdot \hat{\mathbf{u}}_{ij}^{f,m}) - \mathbf{k}^{-1} \mu \hat{\mathbf{u}}_{ij}^{f,m}, \quad (35)$$

subject to the BCs

$$\partial_{\mathbf{n}} \hat{\mathbf{u}}_{ij}^{f,m}|_{\Gamma_{ij}^l} = R_{\Gamma_{ij}^l} [\partial_{\mathbf{n}} \mathbf{u}^{f,m}], \quad (36)$$

$$\hat{p}_{ij}^{f,m}|_{\Gamma_{ij}^l} = R_{\Gamma_{ij}^l} [p^{f,m}], \quad (37)$$

where  $R_{\Gamma_{ij}^l}[\partial_n \mathbf{u}^{f,m}]$  and  $R_{\Gamma_{ij}^l}[p^{f,m}]$  are restrictions of  $\mathbf{u}^{f,m}$  and  $p^{f,m}$  onto  $\Gamma_{ij}^l$ .  $R_{\partial\Omega_{ij}^l}$  is the restriction operator. We solve Eqs. (34) and (35) using the extended SIMPLEC algorithm for compressible flow [30,31].

The local interface problem provides improved BCs for the correction problems in Eqs. (13)–(14) and (21)–(22). Thus, instead of homogeneous BCs in Eqs. (15)–(16) and (23), we have

$$\partial_n \tilde{\psi}^{f,X,m+1}|_{\Gamma_{ij}^{XX}} = R_{\Gamma_{ij}^{XX}}[\partial_n \hat{\mathbf{u}}_{ij}^{f,m}], \quad (38)$$

$$\tilde{\varphi}^{f,X,m+1}|_{\Gamma_{ij}^{XX}} = R_{\Gamma_{ij}^{XX}}[\hat{p}_{ij}^{f,m}] - \langle R_{\Gamma_{ij}^{XX}}[\hat{p}_{ij}^{f,m}] \rangle, \quad (39)$$

where  $\langle R_{\Gamma_{ij}^{XX}}[\hat{p}_{ij}^{f,m}] \rangle$  is the spatial average of  $\hat{p}_{ij}^{f,m}$  over  $\Gamma_{ij}^{XX}$ .

In sections 3.3–3.4, the correction problem accounted for the inhomogeneous terms due to the linearization of the compressible continuity equation. Here, we have modified the correction problem by including boundary residuals. Therefore, the only extra computation for the iterative correction here is to solve the local interface problems. The multiscale solutions after iterative correction are denoted as  $M_1, M_2, \dots$ , with the subscript representing the number of corrective iterations. We outline the algorithm of the multiscale method for compressible flow in Algorithm 1. The above formulation of iterative correction results in a rapid convergence in the multiscale solution, as the reduction of low-frequency modes of error is accelerated via a global problem (see [25] for detailed discussions and the related references [34–36]). We note that other error reduction strategies are available in the MsFV literature, e.g., the fine-scale smoother stages [35,37]. Comparisons with different error reduction strategies are subject to future work.

---

**Algorithm 1** Multiscale method for transient compressible Darcy-Stokes flow.

---

```

1: Set  $flag = 0$  if only single-pass solution ( $M_0$ ) is needed, else  $flag = 1$ 
2: Decompose  $\Omega^P \cup \Omega^M$  into non-overlapping pore grids  $\Omega_i^P$  and microporous grids  $\Omega_i^M$ 
3: Set initial condition for  $S^{f,0} \equiv \{\mathbf{u}^{f,0}, p^{f,0}\}$  at  $t = 0$ 
4: Build local basis functions  $\psi_{ik}^f = \{\psi_{ik}^f, \varphi_{ik}^f\}$  by solving Eqs. (9)–(10) and (18)–(19)
5: for  $n = 0, \dots, N^T$  do ▷ Time loop
6:   Let  $m = 0$ 
7:   while  $\|S^{n+1,m+1} - S^{n+1,m}\| > tol$  do ▷ Iterative correction loop
8:     if  $flag = 1$  then
9:       for  $i = 1, \dots, N_X - 1$  do ▷ Local interface problem loop
10:        for  $j = i + 1, \dots, N_X$  do
11:          Solve the local interface problem on  $\Omega_{ij}^l$  via Eqs. (34)–(35)
12:        end for
13:      end for
14:    end if
15:    for  $j = 1, \dots, N_X$  do ▷ Local correction problem loop
16:      Solve the local correction problem on  $\Omega_i^X$  via Eqs. (13)–(14) and (21)–(22)
17:    end for
18:    Solve the global interface problem in Eq. (31) to obtain  $[p_{ij}^{c,n+1,m+1}]_{N_I \times 1}$ 
19:    Construct the global fine-scale solution  $S^{f,n+1,m+1} \equiv \{\mathbf{u}^{f,n+1,m+1}, p^{f,n+1,m+1}\}$  using Eqs. (32)–(33)
20:    Set  $m = m + 1$ 
21:  end while
22: end for

```

---

### 3.6. Multiscale formulation for incompressible Darcy-Stokes flow

The multiscale method for incompressible flow is simpler because the equations are linear. The continuity equation for both pore and microporous grids is

$$\nabla \cdot \mathbf{u} = 0. \quad (40)$$

The momentum equation for microporous grids is still the Darcy equation. For pore grids, the momentum balance is modeled using the incompressible DBS equation

$$0 = -\nabla p + \frac{\mu}{\phi} \nabla \cdot (\nabla \mathbf{u}) - \mathbf{k}^{-1} \mu \mathbf{u}. \quad (41)$$

The local basis problem for pore grids is

$$\nabla \cdot \psi_i^{f,P} = 0, \quad (42)$$

$$0 = -\nabla \varphi_i^{f,P} + \nabla \cdot (\mu \nabla \psi_i^{f,P}) - \mathbf{k}^{-1} \mu \psi_i^{f,P}, \quad (43)$$

subject to the BCs



$$\partial_{\mathbf{n}} \psi_{ik}^{f,P} |_{\Gamma_{ij}^{PX}} = 0, \quad (44)$$

$$\varphi_{ik}^{f,P} |_{\Gamma_{ij}^{PX}} = \delta_{kj}. \quad (45)$$

The local basis problem for microporous grids is

$$\nabla \cdot \psi_{ik}^{f,M} = 0, \quad (46)$$

$$\psi_{ik}^{f,M} = -\frac{\mathbf{k}}{\mu} \nabla \varphi_{ik}^{f,M}, \quad (47)$$

subject to the BCs

$$\varphi_{ik}^{f,M} |_{\Gamma_{ij}^{MX}} = \delta_{kj}. \quad (48)$$

The global problem is similar to that of compressible flow, with two differences. First, density is constant here so the mass flowrate is equivalent to volumetric flowrate. Second, there is no inhomogeneous term in Eq. (40), so no correction problem (Eqs. (13)–(16) and Eqs. (18)–(23)) is needed to obtain  $M_0$ . The mass flowrates across the interfaces  $\Gamma_{ij}^{XX}$  with  $l \in [1, N_l]$  for arbitrary  $[p_{ij}^c]_{N_l \times 1}$  can be written as (compare to Eq. (27))

$$Q_i^c = G_i^c P_i^c. \quad (49)$$

Imposing continuity of mass flowrate at all the interfaces gives the following global linear system

$$G^c [p_{ij}^c]_{N_l \times 1} = F^{c,b} \quad \forall ij, \quad (50)$$

where  $F^{c,b}$  is the  $N_l \times 1$  RHS vector due to the global BCs. Solving Eq. (50) yields  $[p_{ij}^c]_{N_l \times 1}$ , with which we construct  $M_0$  as

$$\mathbf{u}^f = \sum_{\forall i} \left( \sum_{k \in I_i} p_{ik}^c \psi_{ik}^{f,X} \right), \quad (51)$$

$$p^f = \sum_{\forall i} \left( \sum_{k \in I_i} p_{ik}^c \varphi_{ik}^{f,X} \right). \quad (52)$$

Similar to compressible flow, we can improve  $M_0$  by correcting the local BCs by solving a set of local interface problems on  $\Omega_{ij}^I$ . The iterative correction is identical to section 3.5, except that we now solve Eqs. (40)–(41) on interface grids. Assuming that the global fine-scale solution at iteration  $m$  is known, the interface problem can be written as

$$\nabla \cdot \hat{\mathbf{u}}_{ij}^{f,m} = 0, \quad (53)$$

$$0 = -\nabla \hat{p}_{ij}^{f,m} + \frac{\mu}{\phi} \nabla \cdot \left( \nabla \hat{\mathbf{u}}_{ij}^{f,m} \right) - \mathbf{k}^{-1} \mu \hat{\mathbf{u}}_{ij}^{f,m}. \quad (54)$$

The BCs for Eqs. (53) and (54) at the boundaries of  $\Omega_{ij}^I$  come from the global fine-scale solution  $\mathbf{u}^{f,m}$  and  $p^{f,m}$  and are identical to Eqs. (36)–(37). Given  $\hat{\mathbf{u}}_{ij}^{f,m}$  and  $\hat{p}_{ij}^{f,m}$ , we solve a correction problem that improves the BCs used in building the basis functions  $\psi_{ik}^{f,X} \equiv \{\psi_{ik}^{f,X}, \varphi_{ik}^{f,X}\}$  on  $\Omega_i^X$ .

The correction problem for the pore grid  $\Omega_i^P$  is

$$\nabla \cdot \tilde{\psi}_i^{f,P,m+1} = 0, \quad (55)$$

$$0 = -\nabla \tilde{\varphi}_i^{f,P,m+1} + \nabla \cdot \left( \mu \nabla \tilde{\psi}_i^{f,P,m+1} \right) - \mathbf{k}^{-1} \mu \tilde{\psi}_i^{f,P,m+1}, \quad (56)$$

subject to the BCs

$$\partial_{\mathbf{n}} \tilde{\psi}_i^{f,P,m+1} |_{\Gamma_{ij}^{PX}} = R_{\Gamma_{ij}^{PX}} \left[ \partial_{\mathbf{n}} \hat{\mathbf{u}}_{ij}^{f,m} \right], \quad (57)$$

$$\tilde{\varphi}_i^{f,P,m+1} |_{\Gamma_{ij}^{PX}} = R_{\Gamma_{ij}^{PX}} \left[ \hat{p}_{ij}^{f,m} \right] - \left\langle R_{\Gamma_{ij}^{PX}} \left[ \hat{p}_{ij}^{f,m} \right] \right\rangle. \quad (58)$$

The correction problem for the microporous grid  $\Omega_i^M$  is

$$\nabla \cdot \tilde{\psi}_i^{f,M,m+1} = 0, \quad (59)$$

$$\tilde{\psi}_i^{f,M,m+1} = -\frac{\mathbf{k}}{\mu} \nabla \tilde{\varphi}_i^{f,M,m+1}, \quad (60)$$

subject to the BCs

$$\tilde{\varphi}_i^{f,M,m+1}|_{\Gamma_{ij}^{MX}} = R_{\Gamma_{ij}^{MX}} \left[ \hat{p}_{ij}^{f,m} \right] - \left\langle R_{\Gamma_{ij}^{MX}} \left[ \hat{p}_{ij}^{f,m} \right] \right\rangle. \quad (61)$$

Given  $\tilde{\varphi}_i^{f,X,m+1}$  and  $\tilde{\varphi}_i^{f,X,m+1}$ , the global fine-scale solution at iteration  $m+1$  is constructed via Eqs. (32) and (33) similar to compressible flow. We repeat the above steps for the next iteration until convergence is achieved. The algorithm for the incompressible multiscale method is outlined in Algorithm 2.

---

**Algorithm 2** Multiscale method for incompressible Darcy-Stokes flow.

---

```

1: Set  $flag = 0$  if only single-pass solution ( $M_0$ ) is needed, else  $flag = 1$ 
2: Decompose  $\Omega^P \cup \Omega^M$  into non-overlapping pore grids  $\Omega_i^P$  and microporous grids  $\Omega_i^M$ 
3: Build local basis functions  $\psi_{ik}^f = \{\psi_{ik}^f, \varphi_{ik}^f\}$  by solving Eqs. (42)–(43) and (46)–(47)
4: Solve the global interface problem via Eq. (50) to obtain  $[p_{ij}^{c,0}]_{N_I \times 1}$ 
5: Construct the single-pass global fine-scale solution ( $M_0$ )  $S^{f,0} = \{\mathbf{u}^{f,0}, p^{f,0}\}$  using Eqs. (51)–(52)
6: if  $flag = 1$  then
7:   while  $\|S^{m+1} - S^m\| > tol$  do
8:     for  $i = 1, \dots, N_X - 1$  do
9:       for  $j = i + 1, \dots, N_X$  do
10:        Solve the local interface problem on  $\Omega_{ij}^I$  via Eqs. (53)–(54)
11:      end for
12:    end for
13:    for  $j = 1, \dots, N_X$  do
14:      Solve the local correction problem on  $\Omega_i^X$  via Eqs. (55)–(56) and (59)–(60)
15:    end for
16:    Solve the global interface problem via Eq. (50) to obtain  $[p_{ij}^{c,m+1}]_{N_I \times 1}$ 
17:    Construct the global fine-scale solution  $S^{f,m+1} \equiv \{\mathbf{u}^{f,m+1}, p^{f,m+1}\}$  using Eqs. (32)–(33)
18:  end while
19: end if

```

---

#### 4. Numerical results

We test the multiscale method using three porous medium images: (1) A 2D synthetic ternary image shown in Fig. 1(a); (2) A 2D slice of a 3D image of a shale sample obtained by Focused Ion Beam (FIB)-SEM; (3) A 3D shale image, which is a subvolume of a 3D FIB-SEM image. We present results from both incompressible flow and transient compressible flow for the first two test cases, and only show the incompressible results for the third 3D case.

##### 4.1. Test case 1: Synthetic 2D image

The image we use for the first test case is shown in Fig. 1(a). The white and black colors represent macropores ( $\Omega^P$ ) and non-porous solids ( $\Omega^S$ ), respectively. Gray color denotes regions that have unresolved microporosity ( $\Omega^M$ ). We decompose the image into coarse pore and microporous grids (see Fig. 1(b)) and coarse interface grids (see Fig. 1(c)) using the domain decomposition of section 3.2.

The top and bottom boundaries of the image are no flow boundaries (i.e., walls), and the left and right boundaries are inlet and outlet, respectively. The physical dimensions of the image are  $L_x = 5$  mm and  $L_y = 4$  mm. The fine-scale mesh consists of  $625 \times 500$  uniform grid cells in  $x$  and  $y$  directions. The microporous regions are assumed to be homogeneous and isotropic with a porosity  $\phi = 0.1$  and a permeability  $k = 0.17$  mD. The permeability is computed via the Kozeny-Carman equation (Eq. (62)) with an average pore diameter  $d = 5 \times 10^{-6}$  m.

$$k = \frac{d^2}{180} \frac{\phi^3}{(1 - \phi)^2}. \quad (62)$$

The boundary condition is set to  $\partial_n \mathbf{u} = 0$  and  $p_l = (1.01325 \times 10^5 + 10)$  Pa at the inlet, and  $\partial_n \mathbf{u} = 0$  and  $p_r = 1.01325 \times 10^5$  Pa at the outlet. The pressure change across the domain is  $\Delta p = 10$  Pa. Incompressible flow simulation yields an overall permeability of  $K = 177.8$  D for the sample. Given permeability, we define a characteristic time scale  $t_c$  for compressible flow via

$$t_c = \frac{L_x^2 \phi \frac{\partial \rho}{\partial p}}{\rho K / \mu}. \quad (63)$$

Consider the fluid as an ideal gas, we have  $\rho = pM/(RT_m)$ , where  $M$  is the molecular weight of the gas,  $R$  is the universal gas constant, and  $T_m$  is the absolute temperature. We use  $t_c$  to define dimensionless time  $T = t/t_c$ . A characteristic velocity is defined by  $u_c = l_c^2 \Delta p / (8 \mu L_x)$ , in which  $l_c = 0.3$  mm is a characteristic throat size. We then define the dimensionless velocity as  $U = u/u_c$ . The pressure is nondimensionalized as  $P = (p - p_r) / \Delta p$ .

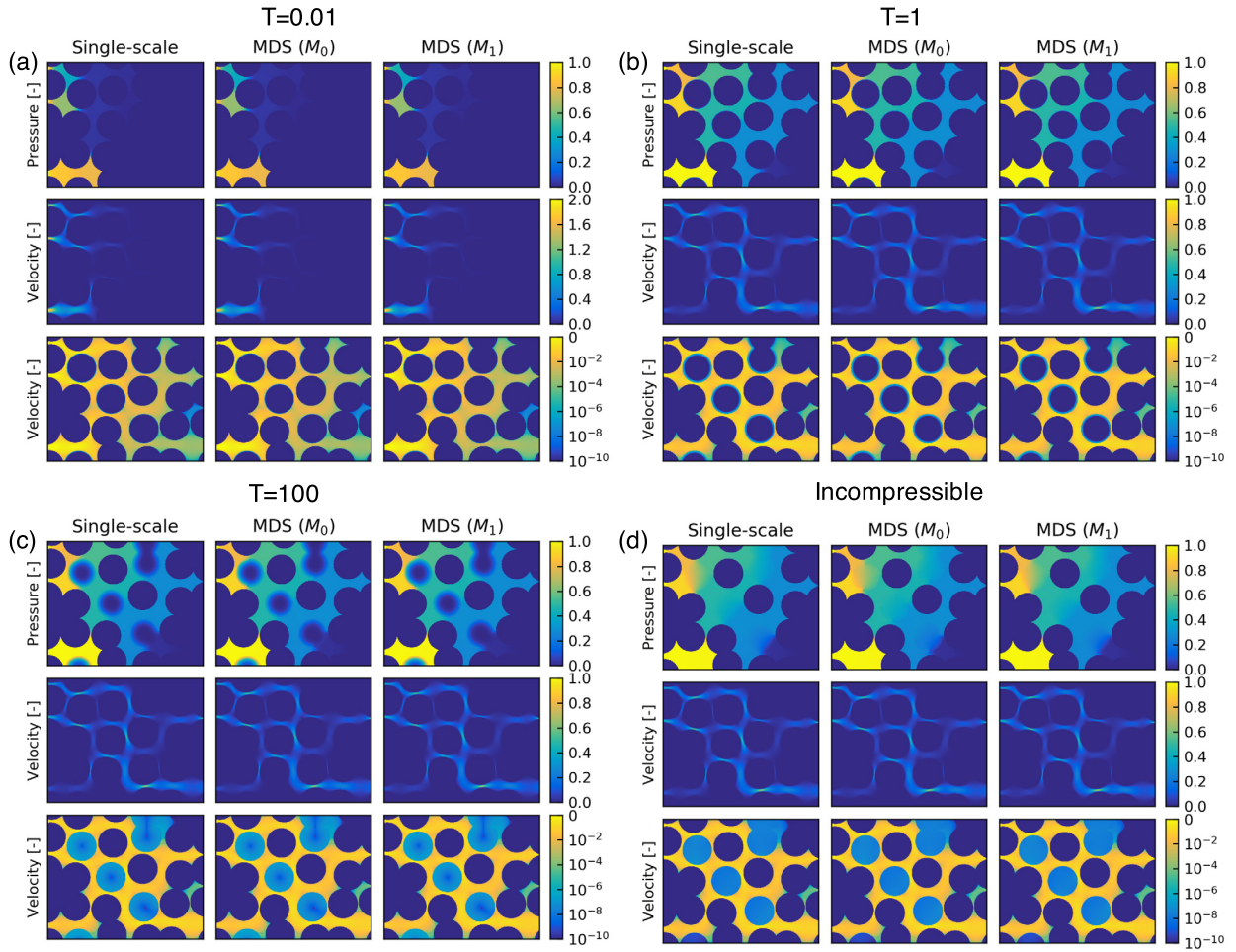


**Fig. 2.** Distribution of pressure and velocity magnitude from the single-scale solution and the multiscale solutions ( $M_0$  and  $M_1$ ). MDS is in short for multiscale Darcy-Stokes. (a–c) Transient solutions of compressible flow for  $T = 0.01, 1, 100$  with pressure shown in the first row, velocity magnitude shown in the second row, and velocity magnitude on a log scale shown in the third row. (d) Incompressible solutions. The color indicates the magnitude as shown in the colorbars. Pressure, velocity, and time are all in dimensionless forms here and in any other figures of this paper.

For incompressible flow,  $M_0$  is in excellent agreement with the single-scale solution (see Fig. 2(d)). Small errors are localized at the interfaces between coarse pore and/or microporous grids. Local errors are eliminated with just one corrective iteration in  $M_1$ . We show comparisons of pressure and velocity magnitude for  $M_0$  and  $M_1$ , and the single-scale solution. Because velocity in the microporous regions is a few orders of magnitude smaller than that in the macropores, we also show velocity magnitudes on a log scale (third row of Fig. 2).

Fig. 2(a–c) compares the transient pressure and velocity magnitude for compressible flow at dimensionless time  $T = 0.01, 1, 100$  obtained from the single-scale and multiscale methods. The agreement between  $M_0$  and the single-scale solution is very good. The multiscale solution after one corrective iteration  $M_1$  significantly reduces the local errors. To measure the difference between multiscale and single-scale solutions, we compute the  $L_2$ -norm of the pointwise errors. Fig. 3 shows the  $L_2$  errors normalized by the maximum pressure/velocity of the single-scale solution. We see that  $M_0$  starts with an error of less than 0.5% for both pressure and velocity, and then quickly drops below 0.1% after one corrective iteration in  $M_1$ . Errors stagnate beyond two iterations. This is because the multiscale errors are reduced to the same order as the fine-scale discretization error (see [25] for a detailed discussion).

#### 4.2. Test case 2: 2D shale image

In the second test case, we use a 2D slice of the 3D FIB-SEM shale image in [14]. The shale image has four material constituents: macropore, organic matter, clay, and granular minerals. The organic matter and clay are considered to be microporous, while the granular minerals are considered to be non-porous and impermeable to flow. For simplicity, we group the organic matter and clay together and assume that they have the same porosity and permeability, which leads to a ternary image with macropores, microporous regions, and non-porous solids (see Fig. 4(a)). We model methane flow

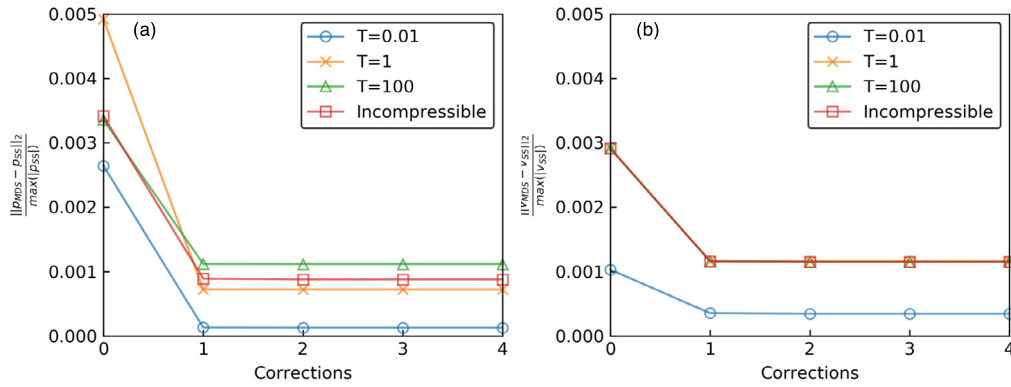


**Fig. 3.**  $L_2$  error of the multiscale method with different number of corrective iterations. (a) and (b) are errors in pressure and velocity magnitude, respectively. We normalize errors by the maximum pressure or velocity magnitude of the single-scale solution.

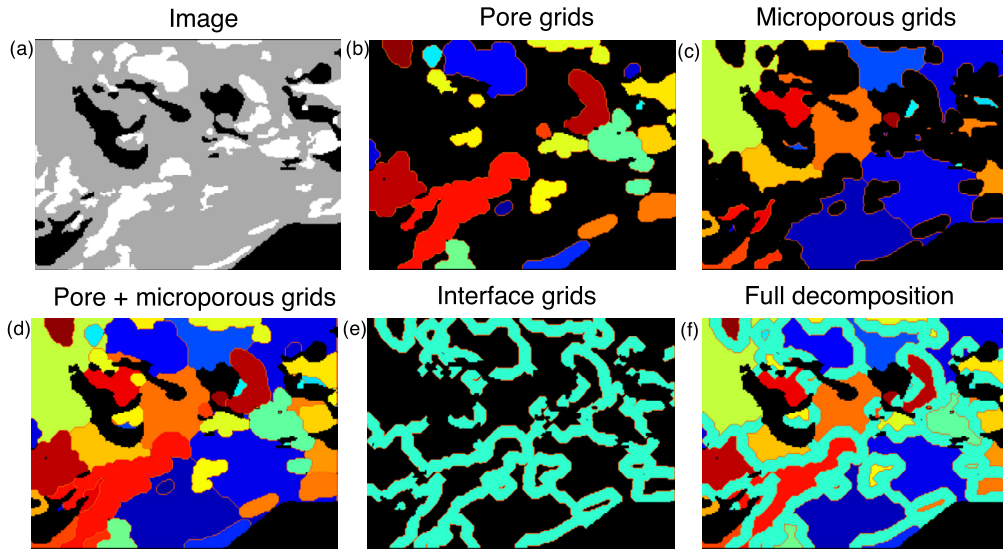


**Fig. 4.** Domain decomposition of a 2D ternary image obtained from a 2D slice of a 3D FIB-SEM shale image. (a) Ternary image where white, gray, and black colors denote macropores, microporous regions, and non-porous solids, respectively. (b) Decomposed pore grids. (c) Decomposed microporous grids. (d) Decomposed pore and microporous grids shown together. (e) Decomposed interface grids. (f) Full decomposition with pore, microporous, and interface grids.

through the image, but neglect adsorption and desorption, and do not consider Knudsen diffusion and slip flow. Similar to test case 1, we assume that the microporous regions are homogeneous and isotropic.

Fig. 4(b–c) show the decomposed pore and microporous grids corresponding to Fig. 4(a), respectively. Combining pore and microporous grids gives Fig. 4(d). Interface grids are shown in Fig. 4(e). Fig. 4(f) shows the full decomposition with the pore, microporous, and interface grids together. The physical dimensions of the image are  $L_x = 2 \mu\text{m}$  and  $L_y = 1.5 \mu\text{m}$ . The pixel size of the image is  $10 \text{ nm} \times 10 \text{ nm}$ . The fine-scale mesh consists of  $400 \times 300$  uniform grid cells in  $x$  and  $y$  directions, which divide each pixel into  $2 \times 2$  cells.

We design two simulation scenarios for this test case. The first is similar to test case 1, where we set a higher pressure at the inlet than the outlet and compute the pressure and velocity distribution for incompressible flow. The inlet BCs are  $\partial_n \mathbf{u} = 0$  and  $p_l = (1.01325 \times 10^5 + 10) \text{ Pa}$ , and the outlet BCs are  $\partial_n \mathbf{u} = 0$  and  $p_r = 1.01325 \times 10^5 \text{ Pa}$ . The second scenario simulates a gas depletion process. We set a higher pressure inside the domain than the outlet and let the gas expand due to the pressure gradient. The inlet is a no flow boundary (i.e., wall). The initial pressure in the domain is  $p = (1.01325 \times 10^5 + 10) \text{ Pa}$ . The outlet BCs are  $p = 1.01325 \times 10^5 \text{ Pa}$  and  $\partial_n \mathbf{u} = 0$ . The porosity and permeability of the microporous region are  $\phi = 0.1$  and  $k = 0.69 \text{ nD}$ , respectively.

For incompressible flow, we compare the pressure and velocity distributions from the multiscale ( $M_0$  and  $M_1$ ) and single-scale methods. The difference is very small as shown in Fig. 5. The incompressible solution yields an overall permeability of  $K = 1.04 \text{ nD}$  for the sample. Similar to test case 1, we define a characteristic time  $t_c$  via Eq. (63) and use it to define the dimensionless time  $T = t/t_c$ . The characteristic velocity is  $u_c = K \Delta p / (\mu L_x)$ , and is used to define the dimen-

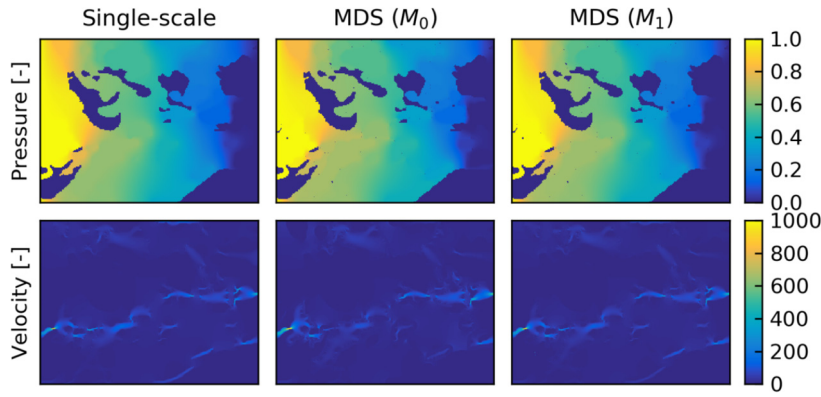


**Fig. 5.** Distribution of pressure and velocity magnitude of the incompressible solutions. The first column represents the single-scale solution and the second and third columns are the multiscale solutions ( $M_0$  and  $M_1$ ). The color indicates the magnitude as shown in the colorbars.

sionless velocity  $U = u/u_c$ . In transient gas depletion under compressible flow, we show pressure and velocity distributions at  $T = 0.001, 0.01, 0.1$ . Fig. 6 shows that the pressure signal propagates from the outlet into the domain. The transient behavior is well-captured by both  $M_0$  and  $M_1$ . We compute the gas production rate at the outlet over time (decline curve) from the single-scale and multiscale methods ( $M_0$  and  $M_{1-4}$ ). The production rate ( $Q = q/q_c$ ) is normalized by the characteristic rate  $q_c = | -A_{yz}K\Delta p/\mu/L_x |$ , where  $A_{yz}$  is the cross-sectional area of the y-z boundary. Fig. 7 shows all decline curves to collapse onto one another with only  $M_0$  being slightly different. This observation is confirmed by the  $L_2$  errors of the multiscale solutions in Fig. 8. The errors start at a few percent in  $M_0$  and then quickly reduce to less than one percent after one iteration in  $M_1$ . Errors keep decreasing with further iterations and finally asymptote at values on the same order as the fine-scale discretization error.

#### 4.3. Test case 3: 3D shale image

In the third test case, we apply the multiscale method to a 3D image (see Fig. 9(a)), which is a subvolume of the 3D shale image from [14]. The image is  $1 \mu\text{m} \times 1 \mu\text{m} \times 1 \mu\text{m}$  with  $100 \times 100 \times 50$  voxels. We perform the same procedure as in test case 2 and convert the image into a ternary image with macropores, microporous regions, and non-porous solids. To avoid round-off errors due to the small length scales, we increase the image size to  $L_x = 1 \text{ cm}$ ,  $L_y = 1 \text{ cm}$ , and  $L_z = 1 \text{ cm}$ . The voxel size is now  $0.01 \text{ cm} \times 0.01 \text{ cm} \times 0.02 \text{ cm}$ . The fine-scale discretization has a one-to-one correspondence to the image voxels. The 3D image is decomposed into pore and microporous grids, and interface grids, for the multiscale computation.

Here, we only compute the incompressible solution to demonstrate that the multiscale method is applicable for complex 3D images. We show the distribution of pressure and velocity from both the single-scale solution and multiscale methods ( $M_0$  and  $M_1$ ).  $M_0$  exhibits local differences compared to the single-scale solution, which are unnoticeable after 1 corrective iteration in  $M_1$  (see Fig. 9(b)). The reduction of error with the number of corrective iterations is shown in Fig. 10. Note that the  $L_2$  error for pressure reduces from  $\sim 10\%$  to  $\sim 6\%$  and then stagnates. The stagnation at 6% is due to the low resolution of the fine-scale discretization, which leads to large truncation errors. The multiscale and the single-scale solutions incur a fine-scale error of  $O(h)$  ( $h$  is the size of the fine-scale cells). So the difference between them is also  $O(h)$ . The accuracy of the multiscale method is further discussed in section 5. Overall, the 3D simulations demonstrate that the multiscale method is applicable to complex 3D images. The method is conducive to parallelization for large high-resolution images.

## 5. Discussion

The multiscale method presented in this paper has a number of computational advantages. It decomposes a large domain consisting of macropores and microporous regions into small subdomains that belong to either the macropores or the microporous regions. Stokes and Darcy flow are solved separately in the macropore and microporous subdomains. This is in contrast to the DBS equation used in the single-scale method, which lumps the two regions into one for the entire domain. Only one fine-scale unknown describes Darcy flow (pressure) as opposed to four in the DBS equation (1 pressure, 3 velocities). The multiscale method is therefore very memory efficient, especially for rock images that have large fractions of microporosity. The local problems are also likely to be better-conditioned than the single-scale problem. In addition, local problems are well-suited for parallelization because they decoupled from each other. Here, the implementation of multiscale method is serial. In test case 1, the wall-clock time of  $M_0$  is 30% less for incompressible simulations and 50% less for transient compressible simulations compared to the single-scale method. Each corrective iteration is 20% to 50% of the computational cost of  $M_0$ . In test case 2, the wall-clock time of  $M_0$  is 50% more for incompressible simulations and four times less for transient simulations compared to the single-scale method. Each corrective iteration is 20% and 100% of the computational cost of  $M_0$  for incompressible and transient compressible simulations, respectively. In test case 3,  $M_0$



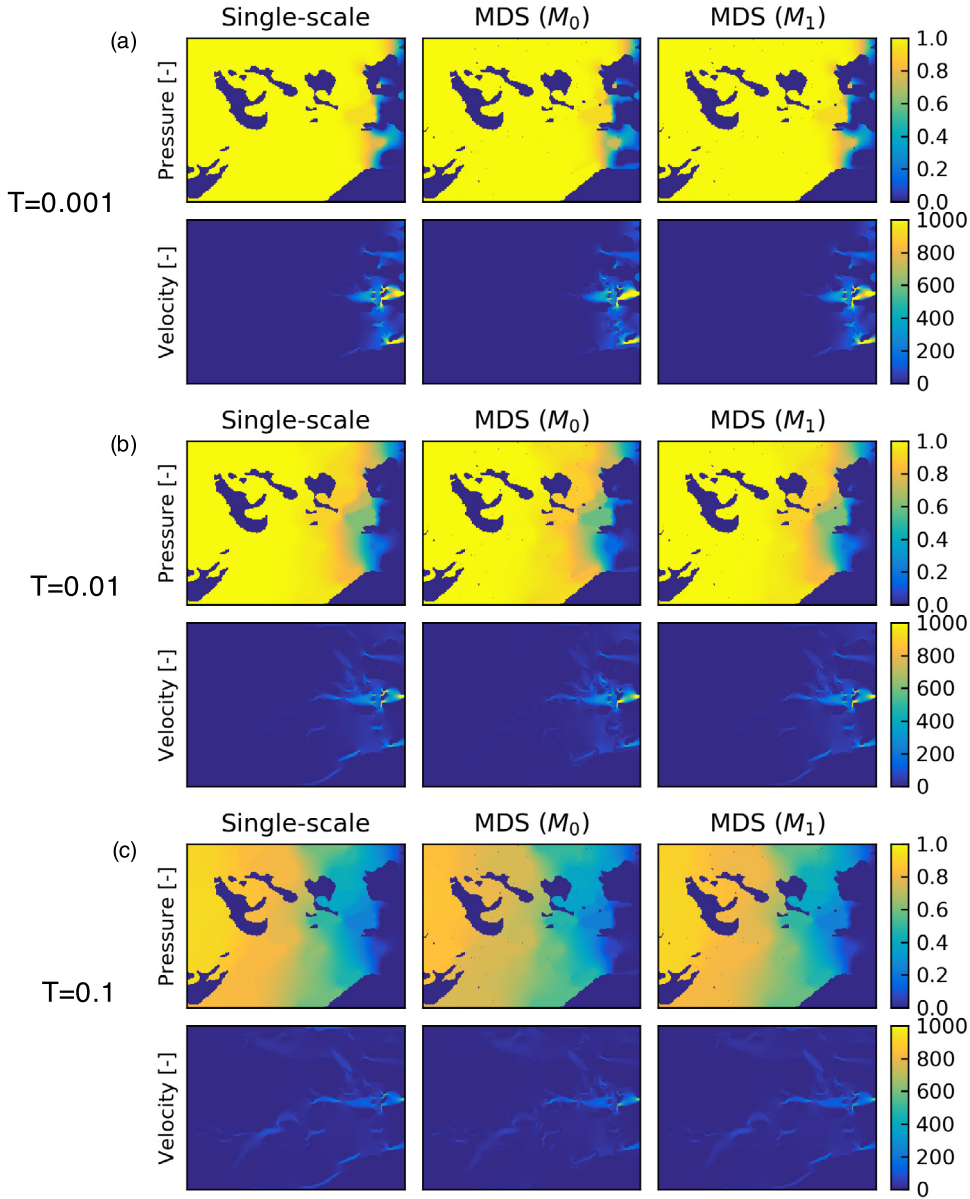


**Fig. 6.** Transient solutions of pressure and velocity at  $T = 0.001, 0.01, 0.1$  during gas depletion under compressible flow. The first column is the single-scale solution, and the second and third columns are the multiscale solutions ( $M_0$  and  $M_1$ ).

is about 4 times slower than the single-scale method. This is due to the large number of neighbors of some subdomains that leads to the construction of a large number of bases. Improved decompositions aimed at minimizing the number of coarse-grid neighbors is subject to future work. Each corrective iteration is 10% of the cost of the  $M_0$  computation. Note that the reported computational costs provide only a rough estimate of the multiscale performance under serial computation. A more rigorous analysis of parallel performance will be conducted in the future.

The multiscale method produces highly accurate initial approximations to single-scale DNS. Its errors quickly drop to less than 1% after one corrective iteration (except for test case 3). The stagnation of multiscale errors after a few iterations is due to differences in the fine-scale discretizations of the single-scale and multiscale methods at  $\Gamma_{ij}^{xx}$ . Namely, the Rhie-Chow interpolation is different leading to residual errors of  $O(h)$  (see [25] for detailed analysis; Appendix B therein). The residual errors disappear as  $h \rightarrow 0$ . Note that the single-scale solution also has a discretization error of  $O(h)$ . In section 4, the residual multiscale errors were less than 0.1% for the first two test cases. In test case 3, the pressure errors asymptote at  $\sim 6\%$ , because the fine-scale discretization  $100 \times 100 \times 50$  (voxel size:  $0.01 \text{ cm} \times 0.01 \text{ cm} \times 0.02 \text{ cm}$ ) is coarse relative to other test cases.

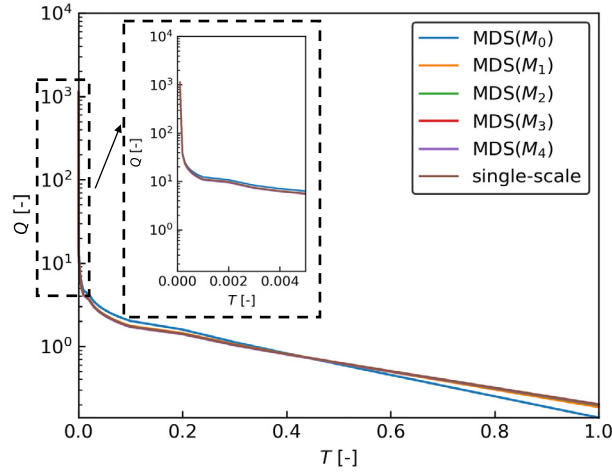


**Fig. 7.** The dimensionless production rates over time from the single-scale solution and the multiscale solutions ( $M_0$  and  $M_{1-4}$ ) on a semi-log plot. The inset shows the production rates at early time when the pressure signal at the outlet has not yet penetrated into the domain, for example, at  $T = 0.001$ , and  $T = 0.01$ .

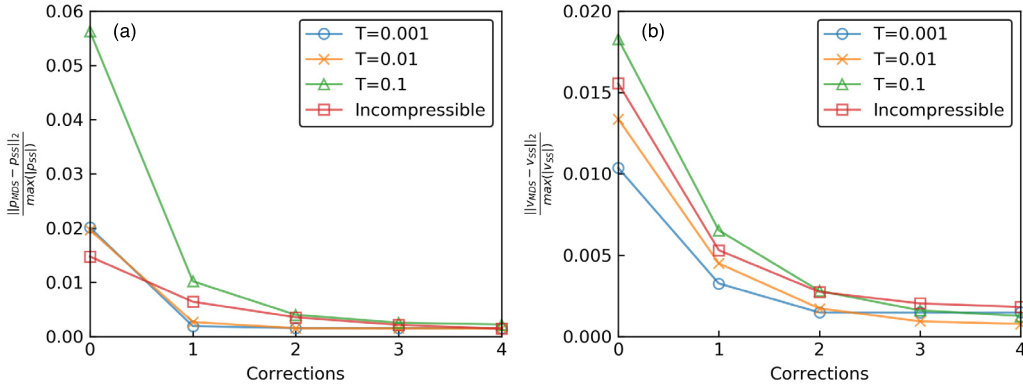


**Fig. 8.**  $L_2$  error of the multiscale solutions with different number of iterative corrections. (a) and (b) are errors for pressure and velocity. The errors are normalized by the maximum pressure or velocity magnitude in the single-scale solution.

Two common approaches are used to couple Darcy and Stokes flow at free flow-porous medium interface. One approach treats the free flow and the porous medium as separate subdomains and couples them through BCs at the free flow-porous medium interface (e.g., [38–40,29,41,42]). Another approach uses a single-momentum equation (i.e., the DBS equation) for both the free flow and the porous medium modified after the Navier-Stokes equation (e.g., [10,43,28,29]). In this work, the second approach was used. Our domain decomposition incorporates a thin layer of microporous region into the pore grids ( $\Omega_i^P$ ) near the interfaces between  $\Omega^P$  and  $\Omega^M$ . Darcy and Stokes flow are therefore coupled inside  $\Omega_i^P$  through the DBS equation. The use of a single momentum equation for the Darcy and Stokes domains ensures continuity of stresses and velocities across the interfaces between free flow and porous medium. It has been shown that the single-momentum equation approach is a good approximation to the explicit coupling of Stokes and Darcy equations using the Beavers-Joseph condition [29].

In the single-momentum equation approach, the standard Rhie-Chow interpolation in co-located schemes may lead to local oscillation of pressure and velocity near the interface between  $\Omega^P$  and  $\Omega^M$  where the porosity and permeability are discontinuous [44,45]. The oscillations are local and do not influence solutions away from the interface, and can be eliminated by a generalized Rhie-Chow scheme that introduces smoothing at the interface [44].

The current implementation of the multiscale method for compressible flow assumes an isothermal system and neglects variations in viscosity with pressure. Therefore, the compressibility only introduces nonlinearity in the continuity equation. The momentum equation is linear. If the variation of viscosity with pressure is considered, an adaptive scheme similar to Jenny et al. [16] in the MsFV may be needed to update the viscosity during the simulation. Other complexities associated with the momentum equation such as pressure dependent permeability for gas flow in organic-rich shale may be handled in a similar fashion.



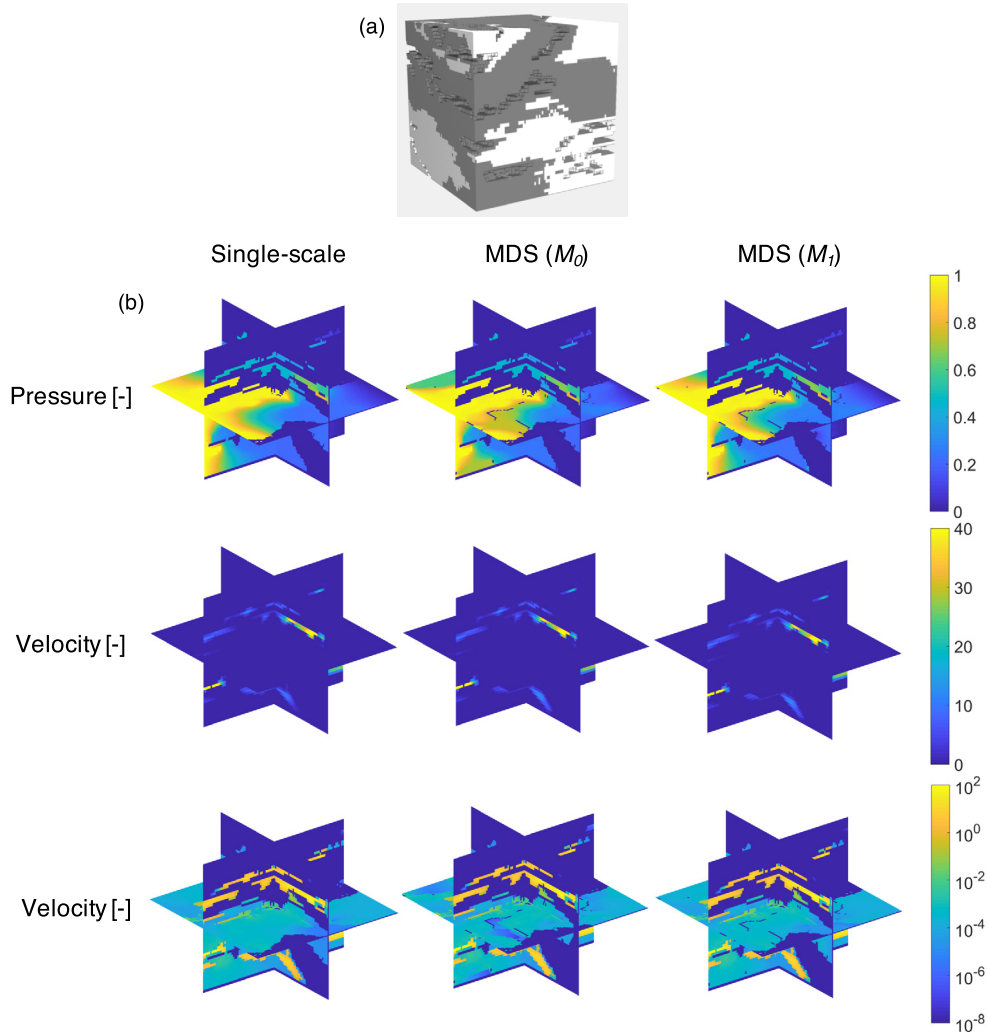


**Fig. 9.** (a) A 3D ternary image where the white color represents non-porous solids, the gray color represents microporous regions, and transparent denotes macropores. (b) Distributions of pressure and velocity magnitude of the incompressible solutions. The first column is the single-scale solutions, and the second and third columns are the multiscale solutions ( $M_0$  and  $M_1$ ). The first and second rows show the pressure and velocity, and the third row shows velocity magnitude on a log scale.

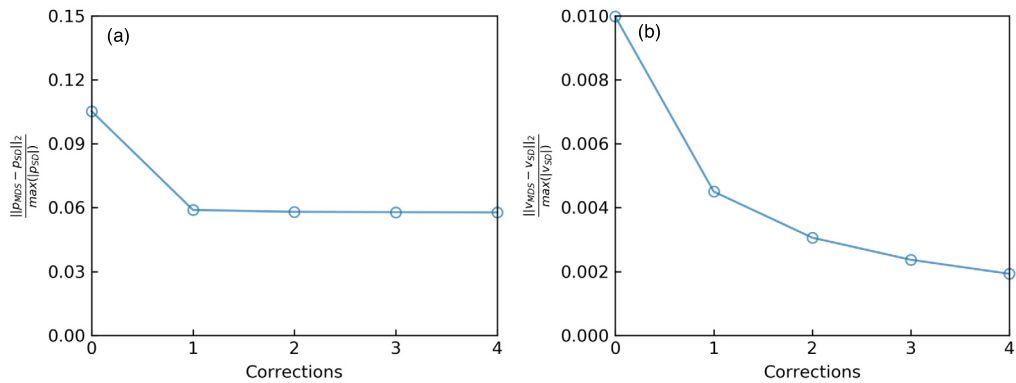


**Fig. 10.**  $L_2$  errors of the multiscale solutions normalized by the maximum pressure or velocity in the single-scale solution. (a) and (b) show the error for pressure and velocity magnitude, respectively.

## 6. Conclusions

We have developed a multiscale method that generalizes PLMM for compressible Darcy-Stokes flow in a segmented ternary porous medium consisting of macropores, microporous regions, and non-porous solids. The multiscale method decomposes the resolved pore space (i.e., macropore) and the subresolution microporous regions into subdomains, where each subdomain belongs either to the macropores or the microporous regions. The nonlinear continuity equation arising from compressibility is linearized using an iterative scheme. We build local basis functions for the macropores and microporous subdomains only once, by solving Stokes and Darcy flow with approximate local BCs. At every iteration, we solve a correction problem at each subdomain to account for the inhomogeneous terms of the linearized continuity equation. A global problem is formulated by imposing continuity of mass flowrate at subdomain interfaces to obtain the basis multipliers. We then construct an approximate global fine-scale solution. The iteration produces an approximate global fine-scale solution (i.e., the single-pass solution  $M_0$ ).  $M_0$  is very accurate and can be further improved through an iterative strategy. We show that one corrective iteration reduces multiscale errors by roughly one order of magnitude ( $<1\%$ ). The corrective iteration is very efficient, with each  $\sim 10\%$ – $50\%$  of the computational cost of  $M_0$ . The multiscale method provides a computationally efficient approach for solving compressible Darcy-Stokes flow in ternary rock images. The method can be parallelized to handle large high-resolution digital images of rock samples that are statistically representative.

## Acknowledgements

This work is supported in part by TOTAL through the Stanford TOTAL enhanced modeling of source rock (STEMS) project. We thank the Center for Computational Earth & Environmental Science (CEES) at Stanford University for access to computational resources.

## References

- [1] M.J. Blunt, B. Bijeljic, H. Dong, O. Gharbi, S. Iglauer, P. Mostaghimi, A. Paluszny, C. Pentland, Pore-scale imaging and modelling, *Adv. Water Resour.* 51 (2013) 197–216.
- [2] D. Wildenschild, A.P. Sheppard, X-ray imaging and analysis techniques for quantifying pore-scale structure and processes in subsurface porous medium systems, *Adv. Water Resour.* 51 (2013) 217–246.
- [3] M.J. Blunt, *Multiphase Flow in Permeable Media: A Pore-Scale Perspective*, Cambridge University Press, 2017.
- [4] A. Mehmani, M. Prodanović, The effect of microporosity on transport properties in porous media, *Adv. Water Resour.* 63 (2014) 104–119.
- [5] T. Bultreys, L. Van Hoorebeke, V. Cnudde, Multi-scale, micro-computed tomography-based pore network models to simulate drainage in heterogeneous rocks, *Adv. Water Resour.* 78 (2015) 36–49.
- [6] T.D. Scheibe, W.A. Perkins, M.C. Richmond, M.I. McKinley, P.D. Romero-Gomez, M. Oostrom, T.W. Wietsma, J.A. Serkowski, J.M. Zachara, Pore-scale and multiscale numerical simulation of flow and transport in a laboratory-scale column, *Water Resour. Res.* 51 (2015) 1023–1035.
- [7] C. Soulaire, F. Gjetvåg, C. Garing, S. Roman, A. Russian, P. Gouze, H.A. Tchelepi, The impact of sub-resolution porosity of x-ray microtomography images on the permeability, *Transp. Porous Media* 113 (2016) 227–243.
- [8] Q. Lin, Y. Al-Khulaifi, M.J. Blunt, B. Bijeljic, Quantification of sub-resolution porosity in carbonate rocks by applying high-salinity contrast brine using x-ray microtomography differential imaging, *Adv. Water Resour.* 96 (2016) 306–322.
- [9] C. Soulaire, H.A. Tchelepi, Micro-continuum approach for pore-scale simulation of subsurface processes, *Transp. Porous Media* 113 (2016) 431–456.
- [10] H. Brinkman, A calculation of the viscous force exerted by a flowing fluid on a dense swarm of particles, *Flow Turbul. Combust.* 1 (1949) 27.
- [11] G.R. Chalmers, R.M. Bustin, I.M. Power, Characterization of gas shale pore systems by porosimetry, pycnometry, surface area, and field emission scanning electron microscopy/transmission electron microscopy image analyses: examples from the Barnett, Woodford, Haynesville, Marcellus, and Doig units, *Am. Assoc. Pet. Geol. Bull.* 96 (2012) 1099–1119.
- [12] L. Ma, K.G. Taylor, P.D. Lee, K.J. Dobson, P.J. Dowe, L. Courtois, Novel 3d centimetre-to nano-scale quantification of an organic-rich mudstone: the carboniferous bowland shale, northern england, *Mar. Pet. Geol.* 72 (2016) 193–205.
- [13] T. Wu, X. Li, J. Zhao, D. Zhang, Multiscale pore structure and its effect on gas transport in organic-rich shale, *Water Resour. Res.* 53 (2017) 5438–5450.
- [14] B. Guo, L. Ma, H. Tchelepi, Image-based micro-continuum model for gas flow in organic-rich shale rock, *Adv. Water Resour.* 122 (2018) 70–84.
- [15] P. Jenny, S. Lee, H.A. Tchelepi, Multi-scale finite-volume method for elliptic problems in subsurface flow simulation, *J. Comput. Phys.* 187 (2003) 47–67.
- [16] P. Jenny, S.H. Lee, H.A. Tchelepi, Adaptive multiscale finite-volume method for multiphase flow and transport in porous media, *Multiscale Model. Simul.* 3 (2005) 50–64.
- [17] P. Tomin, I. Lunati, Hybrid multiscale finite volume method for two-phase flow in porous media, *J. Comput. Phys.* 250 (2013) 293–307.
- [18] K. Khayrat, P. Jenny, A multi-scale network method for two-phase flow in porous media, *J. Comput. Phys.* 342 (2017) 194–210.
- [19] C. Bernardi, Y. Maday, A.T. Patera, Domain decomposition by the mortar element method, in: *Asymptotic and Numerical Methods for Partial Differential Equations with Critical Parameters*, Springer, 1993, pp. 269–286.
- [20] T. Arbogast, L.C. Cowsar, M.F. Wheeler, I. Yotov, Mixed finite element methods on nonmatching multiblock grids, *SIAM J. Numer. Anal.* 37 (2000) 1295–1315.
- [21] T. Arbogast, G. Pencheva, M.F. Wheeler, I. Yotov, A multiscale mortar mixed finite element method, *Multiscale Model. Simul.* 6 (2007) 319–346.
- [22] M.T. Balhoff, S.G. Thomas, M.F. Wheeler, Mortar coupling and upscaling of pore-scale models, *Comput. Geosci.* 12 (2008) 15–27.
- [23] Y. Mehmani, T. Sun, M. Balhoff, P. Eichhubl, S. Bryant, Multiblock pore-scale modeling and upscaling of reactive transport: application to carbon sequestration, *Transp. Porous Media* 95 (2012) 305–326.
- [24] Y. Mehmani, M.T. Balhoff, Bridging from pore to continuum: a hybrid mortar domain decomposition framework for subsurface flow and transport, *Multiscale Model. Simul.* 12 (2014) 667–693.
- [25] Y. Mehmani, H.A. Tchelepi, Multiscale computation of pore-scale fluid dynamics: single-phase flow, *J. Comput. Phys.* 375 (2018) 1469–1487.
- [26] Y. Mehmani, H.A. Tchelepi, Multiscale formulation of two-phase flow at the pore scale, *J. Comput. Phys.* (2019).
- [27] H. Hajibeygi, P. Jenny, Multiscale finite-volume method for parabolic problems arising from compressible multiphase flow in porous media, *J. Comput. Phys.* 228 (2009) 5129–5147.
- [28] F. Golfier, C. Zarecone, B. Bazin, R. Lenormand, D. Lasseux, M. Quintard, On the ability of a Darcy-scale model to capture wormhole formation during the dissolution of a porous medium, *J. Fluid Mech.* 457 (2002) 213–254.

- [29] B. Goyeau, D. Lhuillier, D. Gobin, M. Velarde, Momentum transport at a fluid–porous interface, *Int. J. Heat Mass Transf.* 46 (2003) 4071–4081.
- [30] J. Van Doormaal, G. Raithby, Enhancements of the simple method for predicting incompressible fluid flows, *Numer. Heat Transf.* 7 (1984) 147–163.
- [31] J.H. Ferziger, M. Peric, *Computational Methods for Fluid Dynamics*, Springer Science & Business Media, 2012.
- [32] S. Beucher, Use of watersheds in contour detection, in: *Proceedings of the International Workshop on Image Processing, CCETT*, 1979.
- [33] C. Serra Jean, *Image Analysis and Mathematical Morphology*, Academic Press, Inc, 1983.
- [34] I. Lunati, P. Jenny, The multiscale finite volume method: a flexible tool to model physically complex flow in porous media, in: *Proceedings of European Conference of Mathematics of Oil Recovery X*, Amsterdam, The Netherlands, 2006.
- [35] H. Hajibeygi, G. Bonfigli, M.A. Hesse, P. Jenny, Iterative multiscale finite-volume method, *J. Comput. Phys.* 227 (2008) 8604–8621.
- [36] V. Dolean, P. Jolivet, F. d ric Nataf, *An Introduction to Domain Decomposition Methods: Algorithms, Theory, and Parallel Implementation*, vol. 144, SIAM, 2015.
- [37] M. Tene, Y. Wang, H. Hajibeygi, Adaptive algebraic multiscale solver for compressible flow in heterogeneous porous media, *J. Comput. Phys.* 300 (2015) 679–694.
- [38] G.S. Beavers, D.D. Joseph, Boundary conditions at a naturally permeable wall, *J. Fluid Mech.* 30 (1967) 197–207.
- [39] P.G. Saffman, On the boundary condition at the surface of a porous medium, *Stud. Appl. Math.* 50 (1971) 93–101.
- [40] L. Payne, B. Straughan, Analysis of the boundary condition at the interface between a viscous fluid and a porous medium and related modelling questions, *J. Math. Pures Appl.* 77 (1998) 317–354.
- [41] K. Mosthaf, K. Baber, B. Flemisch, R. Helmig, A. Leijnse, I. Rybak, B. Wohlmuth, A coupling concept for two-phase compositional porous-medium and single-phase compositional free flow, *Water Resour. Res.* 47 (2011).
- [42] K. Baber, K. Mosthaf, B. Flemisch, R. Helmig, S. Müthing, B. Wohlmuth, Numerical scheme for coupling two-phase compositional porous-media flow and one-phase compositional free flow, *IMA J. Appl. Math.* 77 (2012) 887–909.
- [43] G. Neale, W. Nader, Practical significance of Brinkman's extension of Darcy's law: coupled parallel flows within a channel and a bounding porous medium, *Can. J. Chem. Eng.* 52 (1974) 475–478.
- [44] S. Zhang, X. Zhao, S. Bayyuk, Generalized formulations for the Rhie–Chow interpolation, *J. Comput. Phys.* 258 (2014) 880–914.
- [45] M. Nordlund, M. Stanic, A.K. Kuczaj, E.M. Frederix, B.J. Geurts, Improved PISO algorithms for modeling density varying flow in conjugate fluid–porous domains, *J. Comput. Phys.* 306 (2016) 199–215.